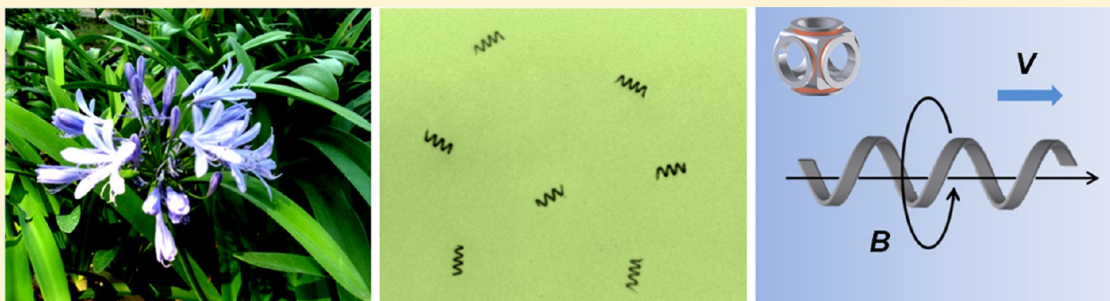


Bioinspired Helical Microswimmers Based on Vascular Plants

Wei Gao, Xiaomiao Feng, Allen Pei, Christopher R. Kane, Ryan Tam, Camille Hennessey, and Joseph Wang*

Department of Nanoengineering, University of California, San Diego, La Jolla, California 92093, United States

S Supporting Information



ABSTRACT: Plant-based bioinspired magnetically propelled helical microswimmers are described. The helical microstructures are derived from spiral water-conducting vessels of different plants, harnessing the intrinsic biological structures of nature. Geometric variables of the spiral vessels, such as the helix diameter and pitch, can be controlled by mechanical stretching for the precise fabrication and consistent performance of helical microswimmers. Xylem vessels of a wide variety of different plants have been evaluated for the consistency and reproducibility of their helical parameters. Sequential deposition of thin Ti and Ni layers directly on the spiral vessels, followed by dicing, leads to an extremely simple and cost-efficient mass-production of functional helical microswimmers. The resulting plant-based magnetic microswimmers display efficient propulsion, with a speed of over 250 $\mu\text{m/s}$, as well as powerful locomotion in biological media such as human serum. The influence of actuation frequencies on the swimming velocity is investigated. Such use of plant vessels results in significant savings in the processing costs and provides an extremely simple, cost-effective fabrication route for the large-scale production of helical magnetic swimmers.

KEYWORDS: Nanomotors, magnetic propulsion, helical, vascular plant, spiral vessels

Synthetic nanomotors represent one of the most exciting research areas in nanotechnology due to their considerable promise for diverse potential biomedical applications.^{1–14} However, propulsion at the nanoscale is extremely challenging due to the absence of inertial forces. The sophistication of man-made micro/nanoscale machines has been increasing rapidly over the past decade, leading to the development of a variety of fuel-driven and fuel-free microscale motors.⁶ Particular attention has been given to chemically powered catalytic micromotors^{15–19} and to magnetically actuated microswimmers.^{20–26} The latter, inspired by the motility of natural microorganisms, are particularly attractive for a variety of future biomedical applications at different scales because they can perform demanding tasks and remote operations while obviating the fuel requirement.^{20–26} Recent advances in magnetically actuated microswimmers have demonstrated considerable potential for performing diverse operations ranging from delivery of therapeutic payloads,²⁷ cell manipulation,^{26,28,29} to nanofabrication.³⁰ Particular attention has been given to helical magnetic microswimmers which can transform the rotation around their helical axis into a translational corkscrew motion under a low-strength rotating magnetic field.^{20–22} However, the large-scale preparation of reproducible three-dimensional helical micro/nanostructures is challenging

and involves complex and expensive fabrication processing techniques, including self-scrolling, glancing angle deposition, and 3-D direct laser writing.^{20–22} The steep instrumental demands of these preparation routes restrict their production only to laboratories with such advanced fabrication facilities and greatly hinder their widespread use. In addition, biocompatible materials are desired for a variety of in vivo biomedical applications.

In contrast to synthetic fabrication techniques, Nature has created uniquely complex patterns and elegant structures through plants over millions of years of evolution. Ranging from the natural fractal geometry of branches³¹ to the formation of barbed raphide crystals³² and thin stacks of grana thylakoids in chloroplasts,³³ plants are capable of generating a variety of highly ordered hierarchical structures on different size scales. At the micrometer and nanometer scales, natural plant structures often have an advanced level of intricacy that rivals the sophistication of current engineered materials and systems.³⁴ Additional synthetic methods can be

Received: October 30, 2013

Revised: November 17, 2013

Published: November 27, 2013

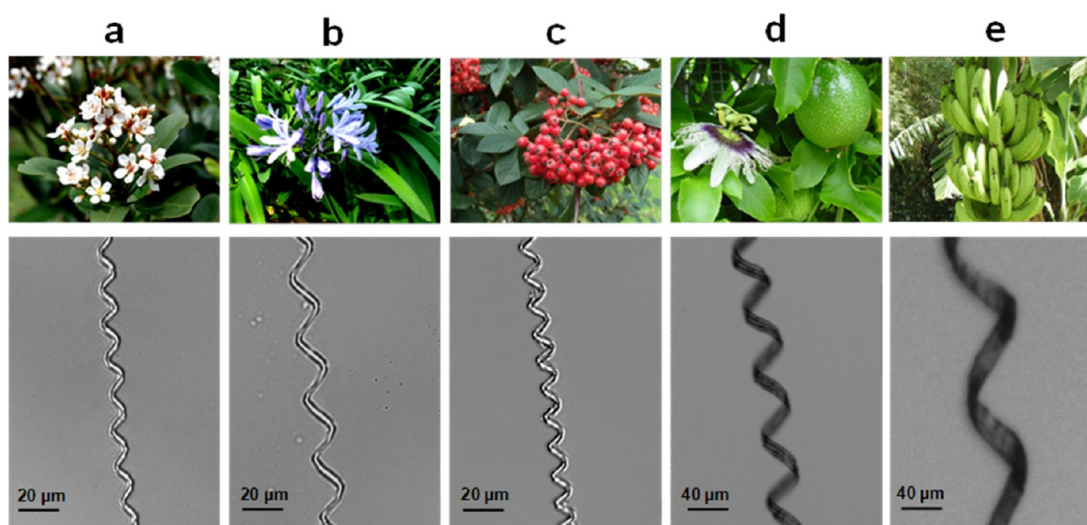


Figure 1. Photographic (upper) and microscopic (lower) images of spiral microstructures from xylem of different plants: (a) *Raphiolepis indica*, (b) *Agapanthus africanus*, (c) *Cotoneaster lacteus*, (d) *Passiflora edulis* (passion fruit), and (e) *Musa acuminata* (banana).

utilized to transform highly structured plant materials into functional materials, taking advantage of their intrinsic natural morphology. These new hybrid structures can be applied to drug delivery,³⁵ environmental remediation,³⁶ energy generation,³⁷ or biotemplated nanofabrication.³⁸ In addition, the direct incorporation of plant structures within polymeric and carbonaceous materials demonstrated high biodegradability, indicating the great promise of plant composites for biomedical³⁹ and biosensing⁴⁰ applications.

Here we demonstrate the first example of plant-based bioinspired magnetically propelled helical microswimmers. The new helical plant vessel-based microswimmers are fabricated by the simple coating of isolated spiral xylem vessel plant fibers with a thin magnetic layer. The intrinsic use of the plant material lends to the biocompatibility and ease of fabrication of the three-dimensional microswimmer, while the magnetic layer allows for high speed propulsion (over 250 $\mu\text{m/s}$) and precise directional control. The new method of using the spiral plant vessel as the major component of the helical micromotor greatly simplifies the fabrication process by utilizing the intrinsic biological microstructures that Nature provides. Due to the extremely high density of spiral vessels within the leaves, over a million individual helical swimmers can be generated from a short single segment of the plant stem.

Xylem tissue extends all throughout vascular plants and transports water and nutrients from the roots to the leaves through capillary action. However, to support the high negative pressures involved in transpirational pull, plants developed thickened and lignin-supported xylem vessel walls.⁴¹ These support structures can consist of chiral crystalline cellulose, resulting in distinct spiral structures of varying dimensions, depending on the type of plant. Figure 1 demonstrates the spiral microstructures from the xylem vessels of a diverse array of vascular plants. Uniform helical microstructures of various diameters can thus be isolated from ordinary plants ranging from decorative shrubs to flowering fruit-bearing trees (a–e). For example, the spiral vessels of the five plants shown in Figure 1 are characterized by a different yet highly reproducible pitch and diameter. The diameters of these structures were found to vary from around 10 μm (e.g., *Raphiolepis*) to over 60 μm (e.g., banana peel).

Additionally, larger vessels are seen to have multiple parallel connected spiral supports, as seen in the larger vessels of the *Passiflora edulis* (passion fruit) and *Musa acuminata* (banana) plants (Figure 1d,e). The plants were taken from the two major classes of vascular angiosperms (flowering plants): *Liliopsida* (monocots) and *Magnoliopsida* (dicots). The distribution of stem vasculature varies between these two classes, with the distinction being drawn between sparsely scattered vascular bundles (monocots) and ring-shaped arrangements of vascular tissue (dicots). In both cases, there are numerous xylem vessels present in the bulk of the stem, allowing for the facile isolation of a large number of spiral microstructures from both dicots (Figure 1a,c,d) and monocots (Figure 1b,e). Control of geometric variables of the spiral vessels, such as the helix diameter and pitch, via mechanical stretching, results in reproducible fabrication and performance of numerous helical microswimmers.

The initial diameter of the unstretched spiral vessel is the most crucial dimension for determining the final shape of the helical structures. Within the leaves, the vessels are initially compressed as tightly wound coils with a characteristic diameter. This helix diameter was found to be consistent for similar leaves in plants of the same species. Isolating the compressed spiral structures from the stem regions of younger, developing leaves of *Raphiolepis indica* resulted in helical coils with diameters within a narrow range of 11.5–12.5 μm . The individual vessel fibers are very thin with radii of 1 μm . We can model the stretching of the helical plant structure as a simple helical spring undergoing plastic deformation with a constant number of helical turns and negligible tensile stretching of the plant fiber. A geometric relationship between the diameter of the helix, D , and the helix angle, θ , can thus be obtained:⁴²

$$\pi D = \pi D_0 \cos \theta \quad (1)$$

where D_0 is the diameter of the helical coil at helix angle 0° . The diameter of the helix can be expressed:

$$D = \frac{1}{\pi} \sqrt{(\pi D_0)^2 - l^2} \quad (2)$$

where l is the helical pitch, or distance between consecutive turns. The diameters of the spiral plant vessels were observed to

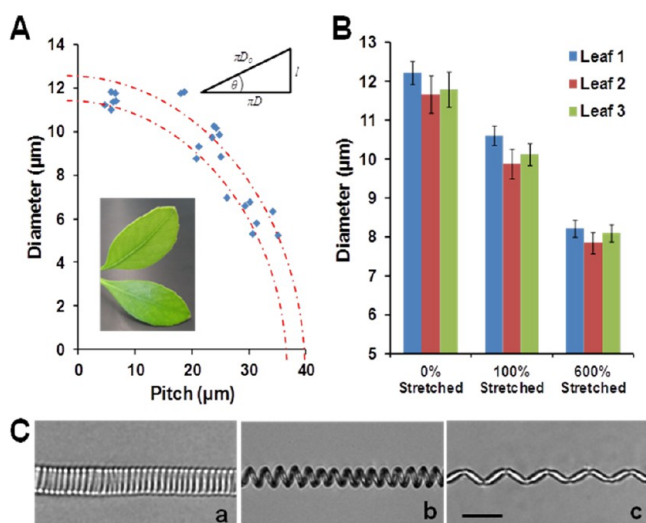


Figure 2. Stretching studies of the helical microstructure from xylem in *R. indica*. (A) The relationship between the pitch and diameter from a single leaf (in red: guides for the eye based on eq 2 for $D_0 = 11.5$ and $12.5 \mu\text{m}$). (B) The relationship of the stretching ratio and the helical diameter for different leaves after different stretching (0%, 100%, and 600%) The error bars represent the standard deviations of the measured diameters found for a sample of $n = 20$ helices at each stretching point. (C) Microscopic images of the spiral vessels isolated from the leaves before stretching (a) and at various stretching states (b,c). Scale bar, $20 \mu\text{m}$.

decrease with increased stretching (Figure 2A,B), following the expected behavior. Further tests on the reproducibility and consistency of the dimensions of the spiral vessels were carried out by evaluating different leaves from different plants. When stretched to 100% and 600% of their initial pitch length, the helical vessels from different leaves had similar diameters, with

the small variability due to the range of initial helix diameters. The resulting stretched spiral vessels are uniform along their length and maintain their mechanical structure (Figure 2C). Thus, the crucial dimensions (i.e., helix diameter) of the spiral vessels can be controlled for the precise fabrication and reproducible performance of helical microswimmers.

To overcome challenges of isolating the spiral vessels through chemical methods,³⁸ we developed a simple yet reproducible extraction method, illustrated in Figure 3A. Leaves of different plant species were lightly scored near the stem perpendicular to the vascular bundles, exposing the coiled spiral vessels. The two leaf segments were then carefully separated, gently drawn apart to a fixed length, and placed upon a narrow glass slide. After creating a large array of helical vessels, thin layers of Ti and Ni were sequentially deposited on the long spiral vessels for improving adhesion and magnetic actuation, respectively. Whenever needed, an external biocompatible layer (e.g., Au or Ti) can be added to address toxicity concerns. These fibers were subsequently embedded within a layer of photoresist or nail polish, then diced into the desired lengths, resulting in a large quantity of identical microswimmers. The helical dimensions of the microswimmers, and the overall shape, remained constant throughout the whole fabrication process. The extremely high density of spiral vessels within the leaves (Figure 3B) provides an ideal platform for mass production of uniform functional helical microswimmers (Figure 3C). This method is thus extremely promising because it provides a simple, cost-effective, and reproducible large-scale mass-production of helical magnetic microswimmers and offers substantial savings in material requirements and processing costs compared to the commonly used methods for fabricating helical microswimmers.^{20–22} For example, for *Rhaphiolepis*, two segments of the lower leaf can each be stretched to obtain 9 mm long vascular fiber bundles, with each ring of vascular bundles containing over 30 spiral vessels. For *Agapanthus*, the

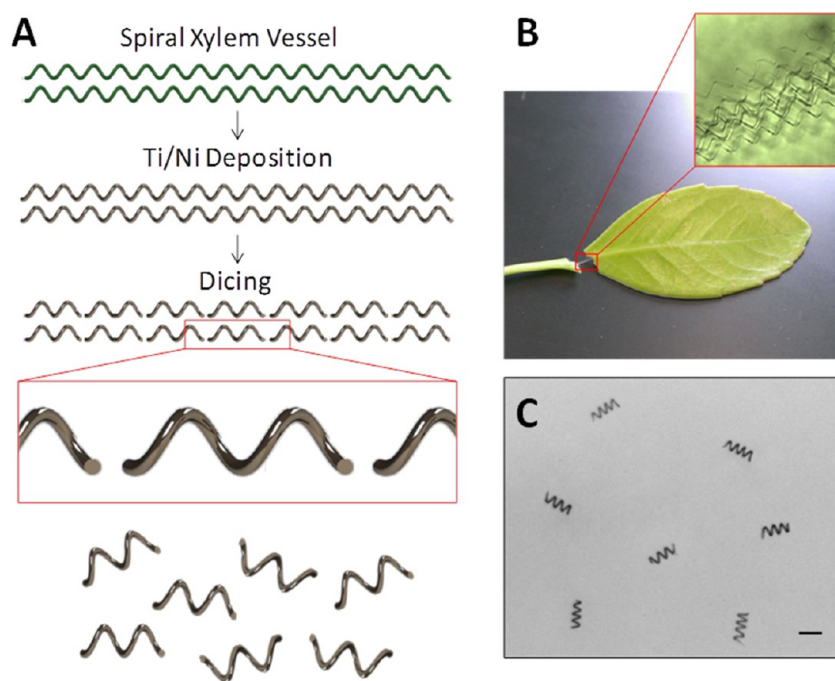


Figure 3. (A) Schematic illustrating the steps involved in the preparation of the plant-based microswimmers. (B) Image illustrating arbitrary stretching of the leaves to isolate the helical structure. The inset optical microscopic image illustrates the high density and uniformity of the natural helices. (C) Microscope image of multiple magnetic helical microswimmers from *A. africanus*. Scale bar, $30 \mu\text{m}$.

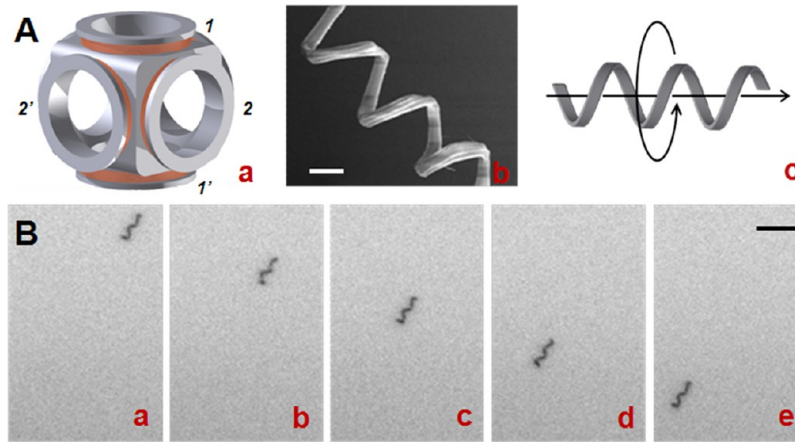


Figure 4. (A, a) The triaxial Helmholtz coil used for generating the rotating magnetic field. (b) SEM image of helical structure of a single microswimmer from *R. indica*. (c) Schematic of the corkscrew motion. Scale bar, 5 μm . (B) Time lapse images depicting efficient propulsion of a helical microswimmer (from the spiral vessel of *R. indica*) under rotating magnetic field (10 G, 70 Hz) over 500 ms time intervals. Scale bar, 50 μm .

flowering stem can have over 300 complete strands of easily extracted spiral vessels. Upon dicing the fibers to 60 μm lengths, one leaf of *Rhaphiolepis* can produce 4500 individual helical swimmers, while a 30 cm segment of *Agapanthus* stem can lead to over 1 500 000 individual helical swimmers.

The precise control of the propulsion of plant-based microswimmer is achieved using three orthogonal Helmholtz coil pairs that create a uniform rotating magnetic field, as illustrated in Figure 4Aa. To characterize the locomotion behavior of the plant-based nanomotors, the helical microswimmers (from *R. indica*, vessel structure shown in Figure 4Ab) were suspended in deionized (DI) water and tested under the magnetic fields with the strength of 10 G and different frequencies ranging from 10 to 80 Hz. At low frequency, the helical swimmers display a wobbling motion, rotating around the axis with a misalignment angle. As the input frequency increases, the angle gradually decreases and finally reaches 0° (corkscrew motion as shown in Figure 4Ac). The time-lapse images in Figure 4B, taken from SI Video 1, illustrate the efficient propulsion of a helical microswimmer (from *R. indica*) with a helix angle of 41° over a 2 s period at 500 ms intervals (a–e) under a rotating magnetic field with a frequency of 70 Hz. The microswimmer is propelled at a high speed of over 250 $\mu\text{m/s}$, which corresponds to a relative speed of ~ 5 body lengths/s. Such efficient propulsion here is comparable to magnetic microswimmers fabricated by the direct laser writing technique and higher than that of most previously reported magnetic swimmers.^{20–26} Similarly, as demonstrated in SI Video 2, the helical swimmer derived from *A. africanus* also displays an efficient speed of around 140 $\mu\text{m/s}$ under the rotating magnetic field with a frequency of 15 Hz.

Based on resistive force theory from slender body dynamics, the drag coefficients of the helical microswimmer can be estimated by:²⁶

$$\xi_{\parallel} = \frac{2\pi\eta}{\ln(2q/r) - 0.5}, \quad \xi_{\perp} = \frac{4\pi\eta}{\ln(2q/r) + 0.5} \quad (3)$$

where ξ_{\parallel} and ξ_{\perp} are the resistive force coefficients parallel and perpendicular to the helical motor axis, q is equal to $0.09l$, r is the radius of the plant vessel fiber, and η is the kinematic viscosity of the fluid. From the simplified model of rotational swimming of a helical motor, the relationship between the externally applied force (F) and torque (τ) and the translational

(v) and rotational (ω) velocities of the motors can be expressed in terms of the propulsion matrix:

$$\begin{bmatrix} F \\ \tau \end{bmatrix} = \begin{bmatrix} a & b \\ b & c \end{bmatrix} \begin{bmatrix} v \\ \omega \end{bmatrix} \quad (4)$$

where the components of the propulsion matrix are:²⁶

$$a = 2\pi n R \left(\frac{\xi_{\parallel} \cos^2(\theta) + \xi_{\perp} \sin^2(\theta)}{\sin(\theta)} \right) \quad (5)$$

$$b = 2\pi n R^2 (\xi_{\parallel} - \xi_{\perp}) \cos(\theta) \quad (6)$$

$$c = 2\pi n R^3 \left(\frac{\xi_{\parallel} \sin^2(\theta) + \xi_{\perp} \cos^2(\theta)}{\sin(\theta)} \right) \quad (7)$$

where θ is the helical angle, R is the helical radius, and n is the number of turns of the helix. Since the entire body of the microswimmer is helical and the magnetic field is uniform, the external applied force (F) is equal to zero. As a result, for constant input frequency ω , there is a predicted linear relationship between the actuation frequencies and the translational velocity (v) of the plant-based helical microswimmers. As illustrated in Figure 5, microswimmers with a diameter of 9 μm and a pitch of 25 μm display increasing movement speeds with increasing input frequency of the

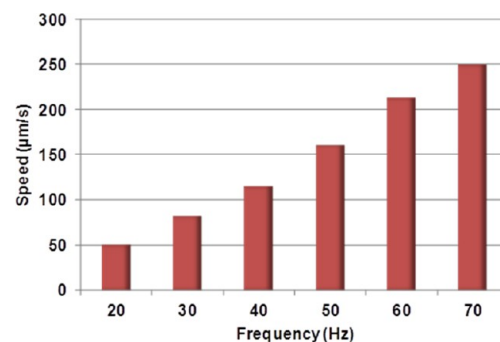


Figure 5. Dependence of the propulsion of plant-derived microswimmers (from *R. indica*) upon the frequencies of the magnetic field (10 G).

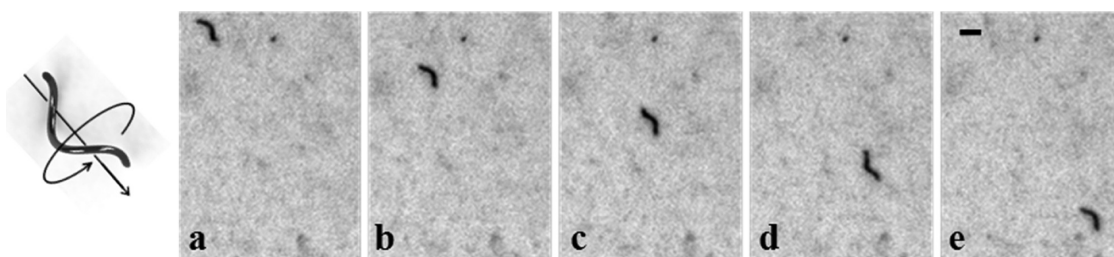


Figure 6. Time lapse images depicting the propulsion of a plant-derived helical microswimmer (from the spiral vessel of *R. indica*) in pure human serum over 600 ms intervals (a–e) using a rotating magnetic field (10 G, 40 Hz). Scale bar, 20 μm .

applied magnetic field. The speed increases linearly from 50 $\mu\text{m/s}$ to 250 $\mu\text{m/s}$ with increasing the applied frequency from 20 to 70 Hz. However, the microswimmer displays a greatly reduced speed at frequencies higher than 80 Hz (step-out frequency). When the frequency is increased above the step-out frequency, the fluidic drag exceeds the maximal available magnetic torque, hence leading to a decrease in velocity as the swimmer rotates out-of-sync with the magnetic field. The linear increase of the speeds of the aforementioned microswimmer matches the theoretical predictions and can be mathematically fit to the theory using the critical frequency ω_c (the frequency at which movement begins) and the step-out frequency ω_{s-o} :⁴³

$$U = \kappa\omega \left(1 - \frac{\omega_c^2}{\omega^2}\right), \quad \omega_c < \omega < \omega_{s-o} \quad (8)$$

where U is the translational velocity, ω is the frequency of the applied rotating magnetic field, and κ is the dimensional coefficient which can be found from numerical data fitting (11/3 in this case). As such, for large enough values of ω , the theory predicts a linear relationship between speed and actuating frequency.

The plant-derived helical microswimmer demonstrates a very fast movement in raw biological media. Figure 6 and the corresponding SI Video 3 illustrate a microswimmer (from *R. indica*) moving in pure human serum at a speed of 85 $\mu\text{m/s}$ under the rotating magnetic field with a frequency of 40 Hz. The absolute speed obtained here is similar to that observed in pure water ($\sim 90 \mu\text{m/s}$), indicating that the increased viscosity of the biological fluid has negligible impact upon the propulsion behavior. This represents a major advantage of the magnetic microswimmer over the common chemically propelled micro/nanomotors whose propulsion is usually hindered by viscous biological media.^{6,16} The microswimmer shown consists of one full helical turn (pitch length 30 μm), displaying a high relative speed of ~ 3 body lengths/s. Such efficient movement of magnetically actuated swimmers in raw biological media is crucial for various relevant biomedical applications requiring precise micromanipulation. It should be noted that at higher frequencies (above 50 Hz), the movement of the plant based-microswimmers in human serum can become punctuated by periods of slower rotational and translational movement.

In conclusion, we have developed a novel plant-derived approach for the high-yield, cost-effective generation of magnetically propelled helical microswimmers. The new bioinspired microswimmers are prepared directly from isolated spiral vessels of plants followed by coating with a magnetic nickel layer. This intrinsic use of the plant material lends to the biocompatibility, biodegradability, and ease of fabrication of the microswimmer, while the magnetic layer allows for high speed propulsion and precise directional control. By harnessing the

intrinsic natural structures of plant xylem vessels, and controlling geometric variables of the spiral vessels (e.g., helix diameter and pitch), this new method provides an extremely simple, cost-effective fabrication route for the large-scale mass-production of defined and effective helical magnetic swimmers compared to common methods for fabricating magnetically actuated helical microswimmers. These plant-derived helical microswimmers are able to be propelled at high speeds in pure human serum, which indicates great promise for future biomedical applications.

Fabrication of the Helical Microswimmers. Various species of plants were collected from the UC San Diego campus (La Jolla, CA). To obtain unstretched spiral vessels, leaves were macerated in a 15 wt % KOH solution at 100 $^{\circ}\text{C}$. After washing off all loose plant matter with pure water, the resulting planar networks of “feather-veins” were gently separated by tweezers to expose isolated, compressed spiral vessels. To obtain stretched spiral vessels, leaves were gently scored, and the two segments were pulled apart to a fixed length. These helical vessels were placed onto glass slides and coated with a 20 nm titanium layer at 1 \AA/s , and a 80 nm nickel layer at 2 \AA/s , using a Temescal BJD 1800 E-beam evaporator. The metal-coated spiral vessels were then embedded within a layer of nail polish or S1818 photoresist and baked at 80 $^{\circ}\text{C}$ for 2 min in order to confine the helices and to protect their structure during dicing. The resulting photoresist film on glass was then diced to desired lengths. After dissolving the protective coating and washing the microswimmers in acetone, the microswimmers were redispersed in DI water. Details of the fabrication protocol are displayed in Figure 3.

Equipment and Experimental Procedure. The homogeneous rotating magnetic field was achieved by a triaxial Helmholtz coil (Figure 4Aa). The magnetic induction was measured using a Gaussmeter (model 475 DSP Gaussmeter, Lake Shore Cryotronics, Inc., Westerville, OH). Videos were captured by an inverted optical microscope (Nikon Instrument Inc. Ti-S/L100), coupled with 10 \times and 4 \times objectives and a Hamamatsu digital camera C11440 using the NIS-Elements AR 3.2 software. Human serum from human male AB plasma was received from Sigma-Aldrich (St. Louis, MO).

■ ASSOCIATED CONTENT

📄 Supporting Information

Videos of the propulsion of the microswimmers. This material is available free of charge via the Internet at <http://pubs.acs.org>.

■ AUTHOR INFORMATION

Corresponding Author

*E-mail: josephwang@ucsd.edu.

Author Contributions

W.G., X.F., and A.P. contributed equally.

Notes

The authors declare no competing financial interest.

ACKNOWLEDGMENTS

This project received support from the Defense Threat Reduction Agency—Joint Science and Technology Office for Chemical and Biological Defense (grant no. HDTRA1-13-1-0002). W.G. is a HHMI International Student Research fellow. X.M.F. acknowledges financial support from Jiangsu Overseas Research & Training Program (China).

REFERENCES

- (1) Mallouk, T. E.; Sen, A. *Sci. Am.* **2009**, *5*, 72–77.
- (2) Wang, J. *ACS Nano* **2009**, *3*, 4–9.
- (3) Mirkovic, T.; Zacharia, N. S.; Scholes, G. D.; Ozin, G. A. *ACS Nano* **2010**, *4*, 1782–1789.
- (4) Mei, Y. F.; Solovev, A. A.; Sanchez, S.; Schmidt, O. G. *Chem. Soc. Rev.* **2011**, *40*, 2109–2119.
- (5) Nelson, B. J.; Kaliakatsos, I. K.; Abbott, J. J. *Annu. Rev. Biomed. Eng.* **2010**, *12*, 55–85.
- (6) Wang, J. *Nanomachines: Fundamentals and Applications*; Wiley-VCH: Weinheim, Germany, 2013.
- (7) Patra, D.; Sengupta, S.; Duan, W.; Zhang, H.; Pavlick, R. A.; Sen, A. *Nanoscale* **2013**, *5*, 1273–1283.
- (8) Solovev, A. A.; Sanchez, S.; Pumera, M.; Mei, Y. F.; Schmidt, O. G. *Adv. Funct. Mater.* **2010**, *20*, 2430–2435.
- (9) Wang, J.; Gao, W. *ACS Nano* **2012**, *6*, 5745–5751.
- (10) Sanchez, S.; Pumera, M. *Chem.-Asian J.* **2009**, *4*, 1402–1410.
- (11) Wang, W.; Duan, W.; Ahmed, S.; Mallouk, T. E.; Sen, A. *Nano Today* **2013**, *8*, 531–554.
- (12) Pumera, M. *Nanoscale* **2010**, *2*, 1643–1649.
- (13) Loget, G.; Kuhn, A. *Nat. Commun.* **2011**, *2*, 535.
- (14) Loget, G.; Kuhn, A. *J. Am. Chem. Soc.* **2010**, *132*, 15918–15919.
- (15) Paxton, W. F.; Kistler, K. C.; Olmeda, C. C.; Sen, A.; St. Angelo, S. K.; Cao, Y.; Mallouk, T. E.; Lammert, P. E.; Crespi, V. H. *J. Am. Chem. Soc.* **2004**, *126*, 13424–13431.
- (16) Mei, Y. F.; Huang, G. S.; Solovev, A. A.; Urena, E. B.; Monch, I.; Ding, F.; Reindl, T.; Fu, R. K. Y.; Chu, P. K.; Schmidt, O. G. *Adv. Mater.* **2008**, *20*, 4085–4090.
- (17) Gao, W.; Sattayasamitsathit, S.; Orozco, J.; Wang, J. *J. Am. Chem. Soc.* **2011**, *133*, 11862–11864.
- (18) Gibbs, J. G.; Kothari, S.; Saintillan, D.; Zhao, Y. P. *Nano Lett.* **2011**, *11*, 2543–2550.
- (19) Wang, W.; Duan, W.; Ayusman, S.; Mallouk, T. E. *Proc. Natl. Acad. Sci. U.S.A.* **2013**, *110*, 17744–17749.
- (20) Zhang, L.; Abbott, J. J.; Dong, L. X.; Kratochvil, B. E.; Bell, D.; Nelson, B. J. *Appl. Phys. Lett.* **2009**, *94*, 064107.
- (21) Ghosh, A.; Fischer, P. *Nano Lett.* **2009**, *9*, 2243–2245.
- (22) Tottori, S.; Zhang, L.; Qiu, F.; Krawczyk, K. K.; Franco-Obregon, A.; Nelson, B. J. *Adv. Mater.* **2012**, *24*, 811–816.
- (23) Ghosh, A.; Fischer, P. *Nanoscale* **2011**, *3*, 557–563.
- (24) Gao, W.; Sattayasamitsathit, S.; Manesh, K. M.; Weihs, D.; Wang, J. *J. Am. Chem. Soc.* **2010**, *132*, 14403–14405.
- (25) Pak, O. S.; Gao, W.; Wang, J.; Lauga, E. *Soft Matter* **2011**, *7*, 8169–8181.
- (26) Peyer, K. E.; Zhang, L.; Nelson, B. J. *Nanoscale* **2013**, *5*, 1259–1272.
- (27) Gao, W.; Kagan, D.; Pak, O. S.; Clawson, C.; Campuzano, S.; Chuluun-Erdene, E.; Shipton, E.; Fullerton, E. E.; Zhang, L.; Lauga, E.; Wang, J. *Small* **2012**, *8*, 460–467.
- (28) Petit, T.; Zhang, L.; Peyer, K. E.; Kratochvil, B. E.; Nelson, B. J. *Nano Lett.* **2012**, *12*, 156–160.
- (29) Zhang, L.; Petit, T.; Peyer, K. E.; Nelson, B. J. *Nanomed.-Nanotechnol. Biol. Med.* **2012**, *8*, 1074–1080.
- (30) Manesh, K. M.; Campuzano, S.; Gao, W.; Lobo-Castañón, M. J.; Shitanda, I.; Kiantaj, K.; Wang, J. *Nanoscale* **2013**, *5*, 1310–1314.
- (31) Morse, D. R.; Lawton, J. H.; Dodson, M. M.; Williamson, M. H. *Nature* **1985**, *314*, 731–733.
- (32) Franceschi, V.; Nakata, P. *Annu. Rev. Plant Biol.* **2005**, *56*, 41–71.
- (33) Staehelin, L. *Photosynth. Res.* **2003**, *76*, 185–196.
- (34) Zhou, H.; Fan, T.; Zhang, D. *ChemSusChem* **2011**, *4*, 1344–1387.
- (35) Hall, S.; Bolger, H.; Mann, S. *Chem. Commun.* **2003**, 2784–2785.
- (36) Bessekhouad, Y.; Robert, D.; Weber, J. V. *J. Photochem. Photobiol., A* **2004**, *163*, 569–580.
- (37) Zhao, Y.; Wei, M.; Lu, J.; Wang, Z. L.; Duan, X. *ACS Nano* **2009**, *3*, 4009–4016.
- (38) Kamata, K.; Suzuki, S.; Ohtsuka, M.; Nakagawa, M.; Iyoda, T.; Yamada, A. *Adv. Mater.* **2011**, *23*, 5509–5513.
- (39) Shibata, M.; Oyamada, S.; Kobayashi, S.; Yaginuma, D. *J. Appl. Polym. Sci.* **2004**, *92*, 3857–3863.
- (40) Wang, J.; Lin, M. S. *Anal. Chem.* **1988**, *60*, 1545–1548.
- (41) Sperry, J. *Int. J. Plant Sci.* **2003**, *164*, S115–S127.
- (42) Johnson, W.; Yu, T. X. *J. Strain Anal. Eng.* **1981**, *16*, 111–121.
- (43) Morozov, K. I.; Leshansky, A. M. *Nanoscale* **2013**, DOI: 10.1039/C3NR04853E.